AGU PUBLICATIONS

JGR

Journal of Geophysical Research: Atmospheres

RESEARCH ARTICLE
10.1002/2014JD022085

Key Points:
- Characterization of ground-based and elevated temperature inversions in a valley
- Microwave temperature remote sensing of lower atmospheric temperature structure
- Connection between inversions and urban air pollution

Correspondence to:
T. Wolf,
tobias.wolf@nersc.no

Citation:
Wolf, T., I. Esau, and J. Reuder (2014), Analysis of the vertical temperature structure in the Bergen valley, Norway, and its connection to pollution episodes, *J. Geophys. Res. Atmos.*, *119*, 10,645–10,662, doi:10.1002/2014JD022085.

Received 28 MAY 2014
Accepted 21 AUG 2014
Accepted article online 26 AUG 2014
Published online 22 SEP 2014

Analysis of the vertical temperature structure in the Bergen valley, Norway, and its connection to pollution episodes

Tobias Wolf[1], Igor Esau[2], and Joachim Reuder[3]

[1]Nansen Environmental and Remote Sensing Center, Bergen, Norway, [2]Nansen Environmental and Remote Sensing Center/Bjerknes Centre for Climate Research, Bergen, Norway, [3]Geophysical Institute, University of Bergen, Bergen, Norway

Abstract The vertical temperature profile in the lowest 1000 m of the atmosphere determines a number of important physical processes and meteorological phenomena such as high concentrations of anthropogenic air pollutants in urban areas. Long-term monitoring of temperature profiles at high vertical and temporal resolution has only become feasible only recently with the introduction of affordable angular scanning microwave temperature profile radiometers. In this study, we analyzed 2 years of continuous temperature profile measurements with the MTP-5HE instrument in the urbanized coastal Bergen valley, Norway. The data have a 10 min temporal and 50 m vertical spatial resolution, thus, constituting a unique data set for a microclimatic characterization of the atmosphere in this high-latitude valley. We studied a 2 year record of ground-based (G-) and elevated (E-) inversions, their dynamics and connection to large-scale circulations, and the links between the urban air quality and the temperature inversions. G-inversions are commonly observed during wintertime nocturnal hours. The local topographic features allow for the frequent occurrence of G-inversions, even during strong winds of up to 16 m/s. E-inversions exist mostly during spring and summer and only during unusual synoptic circulation with large-scale warm air advection directly above the valley. Events with high air pollution, identified based on measurements of NO_2 and particulate matter concentrations, are highly dependent on the existence of G-inversions. Meteorological models poorly capture both G-inversions and E-inversions reducing their utility for the assessment of urban air quality and local weather forecasts.

1. Introduction

High-resolution monitoring of temperature profiles in the Atmospheric Boundary Layer (ABL) is required for many meteorological applications. In particular, early warning and prediction systems for urban air quality depend on accurate and reliable observations of the temperature profiles in the stably stratified ABL (SBL), where the vertical temperature structure is a complex nonmonotonic function of the height above the ground. Severe air pollution episodes have been related to temperature inversions—the profiles with absolute temperature increasing with elevation [e.g., *Ji et al.*, 2012; *Trompetter et al.*, 2013].

Regular monitoring of temperature profiles in urbanized areas can provide valuable information especially at high latitudes [*Kadygrov et al.*, 1999] where SBL cases often cause adverse meteorological conditions with respect to air quality [*Kukkonen et al.*, 2005] that are still difficult to predict [*Fay and Neunhäuserer*, 2006; *Mauritsen et al.*, 2007]. Arguably, in situ measurements of temperature profiles at elevations of a few tens or hundreds of meters above the ground are difficult and costly, if not impossible, in urbanized areas. Satellite remote sensing [e.g., *Wallace and Kanaroglou*, 2009] often does not provide the spatial and temporal resolutions required by the urban air quality community, especially in areas with complex topography. In these circumstances, the relatively inexpensive ground-borne remote sensing techniques like Sound Detection And Ranging systems coupled with radio acoustic sounding system [*Westwater et al.*, 1999] or Passive Microwave Radiometry [*Liou and Yan*, 2006; *Pernigotti et al.*, 2007; *Friedrich et al.*, 2012] may yield better results.

This view motivated the present analysis of the data set obtained with the microwave temperature profiler MTP-5HE from March 2011 through February 2013 in the central Bergen valley (60.4°N, 5.3°E), with a population of about 75,000. This rather complex area has been and still is subject to meteorological research [e.g., *Jonassen et al.*, 2012, 2013; *Valved*, 2012]. The importance of the SBL temperature structure in the Bergen valley was realized decades ago. *Fitje* [1972] used ground-based measurements with weather stations at different heights on the valley slopes. He concluded that such measurements do not resolve the ABL

structure properly, since they were heavily influenced by local effects such as shallow cold layers at the sides of the mountains. *Berge and Hassel* [1984] analyzed temperature inversions using tethered balloon observations over short periods of time. They mostly found inversion top heights of 50 m for short- and 100–120 m for long-lasting inversion episodes and concluded that a drainage wind exists from a small side valley that dominates the wind flow in the valley during inversion episodes.

The interest in temperature profiles and particularly in temperature inversions within the SBL has been revitalized by the sequential occurrence of cold European winters during recent years [*Yang and Christensen*, 2012]. Associated with this, very high concentrations of urban pollutants were frequently recorded in the Bergen area (measurements available online at: www.admin.luftkvalitet.info). Moreover, recent improvements in the theoretical understanding of SBL mixing processes [*Zilitinkevich and Esau*, 2005, 2007], specifically with respect to factors constraining the ABL thickness and hence the trapping of emitted pollutants near the ground, opened the potential to advance the warning and prediction models of air quality hazards. In this understanding the vertical temperature gradient in and above the ABL controls the vertical fluxes of momentum, heat, moisture, and pollution. The temperature gradient above the ABL has previously been omitted in boundary layer models. New models [*Zilitinkevich et al*., 2013] require the vertical temperature gradient as an input parameter, and ground-based remote sensing instruments can provide this.

The aim of this study is to investigate the structure of the lower atmospheric temperature stratification in a high-latitude mountain valley using high-resolution ground-based and remote sensing observations. To do this, we analyze the microwave temperature profiler MTP-5HE data complemented with convenient meteorological observations from Bergen, Norway. We also assess the link between cases of temperature inversions and pollution events with nitrogen dioxide (NO_2), particulate matter with diameter less than 10 μm (PM_{10}), and particulate matter with diameter less than 2.5 μm ($PM_{2.5}$). This study is based on the results of 2 years of continuous monitoring of ABL temperature profiles. It is structured as follows.

Section 2 describes the instrument and the collected data sets. Section 3 contains the meteorological analysis. It is a systematic overview of the frequently occurring inversion episodes. This gives a unique opportunity for model validation and calibration as well as for optimization of the observational network with ground-based remote sensing instruments. Section 3 also describes the link between pollution events and temperature profiles. Finally, section 4 outlines the conclusions.

2. Materials and Methods

2.1. Region of Interest

Bergen (60.4°N, 5.3°E) is the second largest city in Norway. More than 75,000 people reside in the two central districts, located in the elongated Bergen valley that opens toward a sea inlet—Byfjorden in the northwest and toward a large lake and more residential areas in the southwest (Figure 1). The mountains surrounding the valley are between 284 and 643 m high. They protect the valley from storms, significantly reducing the surface layer wind speed [*Jonassen et al*., 2013].

The MTP-5HE instrument is installed on the central tower of the Geophysical Institute (GFI) of the University of Bergen at 45 m above sea level (m asl). The GFI is located at the end of a small ridge in the middle of the valley (Figure 1). It is surrounded by buildings to the north and west, which are at most five stories and lower than the GFI, and a sidearm of the Byfjorden to the south, which is separated from the GFI by a major street. The width of the valley base at the GFI is approximately 1.5 km in northeast to southwest direction.

Most of the time, the ABL in the Bergen valley is well mixed either due to sufficiently strong winds or due to a positive surface heat balance. However, during the winter months, shallow SBLs are frequently observed even during daytime, leading to weak turbulent mixing and increased concentration of pollutants, primarily NO_2 and particulate matter (PM).

2.2. Instrument

The MTP-5HE is a commercially available angular scanning temperature profile radiometer from the Russian producer ATTEX. The same and similar instruments have been used in a number of studies [*Westwater et al*., 1999; *Chang et al*., 2006; *Liou and Yan*, 2006]. The instrument measures brightness temperatures. An inversion algorithm is necessary to obtain the absolute temperature. The inversion algorithm is part of the

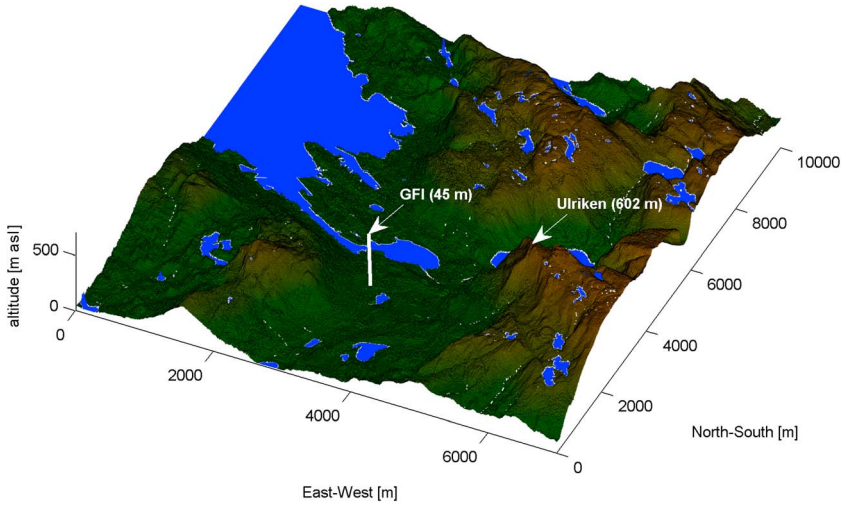

Figure 1. Topographic map of the inner Bergen valley. Data are based on laser scanning measurements. The white, thick line indicates the direction of the MTP-5HE measurements during the horizontal measuring phase and calibration.

software package that comes with the instrument. A detailed validation of this algorithm was out of the scope of this study. The algorithm itself has been amply described by, e.g., *Troitsky et al.* [1993] and *Kadygrov and Pick* [1998]. The general principles of microwave radiometers are described in *Scanzani* [2010]. Possible problems with the usage of microwave radiometers on an operational basis were examined by *Loehnert and Maier* [2012]. At this point we only give a very short summary of the instrument specifications provided by the producer and from the above mentioned references.

The instrument measures the microwave radiation at different elevation angles with a central frequency of 56.6 GHz, a sensitivity of 0.07 K at 1 s integration time, and a bandwidth of 400 MHz. From the angular brightness temperature measurements the temperature profile is automatically calculated and stored. The vertical range of the measurements is 1000 m. The effective vertical resolution is 50 m between 0 and 100 m, 70 m between 100 and 400 m, 80 m between 400 and 600 m, and 120 m between 600 and 1000 m. All measurements are interpolated with a grid spacing of 50 m. The interpolation in the lowest 100 m has been changed part way through the study to have a vertical grid spacing of 25 m. For consistency, we only used the measurements at the 50 m vertical grid spacing. The interval between two measurements can be chosen freely, but a measurement cycle takes at least 180 s. We set this interval to 300 s, meaning that the instrument is in idle mode for 120 s. The inversion algorithm of the brightness temperature measurements is restricted by a calibration of the brightness temperature at 0° elevation angle against an external calibration source (thermometer), which is due to practical reasons mounted on a small mast a few meters away from the instrument, approximately 0.5 m above the instrument. The accuracy of the external calibration thermometer is given by the manufacturer as 0.5 K. The typical mean deviation of the MTP-5HE temperature profile from the actual temperature profile is 0.3 K (0–500 m) to 0.4 K (500–1000 m) and 0.8 K (0–500 m) to 1.2 K (500–1000 m) under adiabatic and inversion conditions, respectively. The performance of the MTP-5HE with a 50 m vertical grid resolution has been validated against radio soundings by *Kadygrov et al.* [2005] during a 1 month period from March to April 2004. The reported vertically and temporally averaged deviations from the radiosondes profiles of $-0.44\,\mathrm{K} \pm 0.76\,\mathrm{K}$ and $0.22\,\mathrm{K} \pm 0.81\,\mathrm{K}$ under adiabatic and inversion conditions fall within the above given range.

2.3. Data Sets

This study is based on a 2 year data set of measurements with the MTP-5HE between March 2011 and February 2013. The data set consists of temperature profiles measured every 5 min with a vertical resolution of 50 m between 45 m and 1045 m asl. We averaged each two successive measurements in order to be consistent in the time stepping with the other meteorological data. We started the nearly continuous operation of the MTP-5HE in February 2011, with only a few shorter breaks (generally a few hours) for maintenance stops. In addition, a few data gaps existed in early 2013 due to a malfunction of the Personal Computer connected to the instrument.

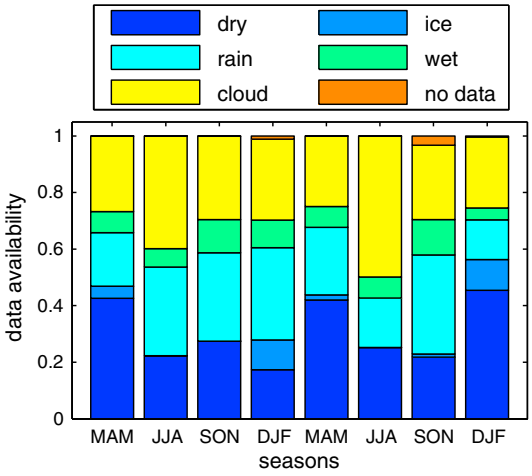

Figure 2. Attribution of MTP-5HE measurements into classes for March 2011 to February 2013. Missing data due to maintenance stops and data removed as unphysical are marked as "no data." Valid data are marked as "dry."

The reliability of MTP-5HE temperature profiles is low during meteorological conditions with high concentrations of liquid water or ice in the optical path of the instrument [*Esau et al*., 2013]. Such situations include rain, a wet radio dome after rain, low-level clouds or fog, and snow or ice both as precipitation and frozen to the radio dome. We removed measurements taken during such conditions. In addition, we removed obviously unphysical measurements that occurred during only a few time steps in the 2 years of operation. The attribution of the MTP-5HE measurements to the relevant meteorological conditions is shown in Figure 2. Measurements marked as dry represent the final, quality-controlled data set. In total only approximately 30% of the measurements fell within this category, illustrating that the measurement method is only of limited use for general statistics of the ABL temperature profiles, in particular, for the climatic conditions prevailing in Bergen. However, this should only have a little effect on the conclusions drawn here. Low clouds, precipitation, and heavy fog, which are the main reasons for most of the dismissed data, suppress radiative cooling and in turn the formation of ABL temperature inversions, which are the focus of this study.

To identify unfavorable meteorological conditions we used 10 min averaged temperature and relative humidity measurements from two automatic meteorological stations (AMS) and rain-rate measurements from an upward pointing micro rain radar (MRR) from the German producer Metek (a description of both can be found at http://www.uib.no/rg/meten/research/continuous-measurements). One of the AMS, hereafter referred to as the GFI AMS, was mounted on top of the same mast as the external calibration source approximately 4 m above the MTP-5HE. The MRR was located on the same roof as the MTP-5HE and the GFI AMS. The second AMS was located on Mount Ulriken at 602 m asl, approximately 3 km east from the GFI (marked in Figure 1).

The AMS data were 10 min averages. The MRR provided 1 min averages that we also averaged to 10 min. To account for noise in the MRR measurements we considered MTP-5HE measurements as rain or snow influenced when the rain rates from the MRR exceeded 0.02 mm/h between 45 and 645 m asl. After each rain event we considered the radio dome as wet for 30 min. To account for icing of the radio dome we extended this period to 1 h when the temperature at the external thermometer of the MTP-5HE was below +1°C. This should be enough to allow loose snow or ice to glide off the radio dome during rotation. Long-term icing events were reported during the routine morning control of all instruments at the GFI (only during Norwegian work days), and the ice cover was removed manually. We further considered measurements as cloud influenced when the relative humidity (RH) at either of the AMS exceeded 95%. No information existed on RH beyond 602 m asl; hence, temperature profiles above that height are less reliable.

Orographic clouds at Ulriken caused an overestimation of the cloud-affected measurements just like icing of the humidity sensor, especially at the Ulriken AMS. That occasionally generated extended periods of 100% RH. The RH sensor of the Ulriken AMS was malfunctioning from 22 July to 2 September 2011, when the sensor was replaced. Some short periods of faulty data continued to exist after that. We generally considered missing or faulty RH or rain data as potentially biased and flagged them as cloud or rain events, leading to a long data gap between July and September 2011. In addition, the RH sensor of the Ulriken AMS occasionally produced single faulty measurements. To reduce the resulting number of interruptions in the MTP-5HE data set, measurements with RH $>$ 95% during one step and with RH $<$ 85% during the time step before and afterward were not removed from our analysis. Figure 3 shows the resulting availability of the AMS data.

For an attribution of temperature inversions to characteristic local wind regimes, we used the wind speed and wind direction at both AMS. To account for icing of the wind sensors, we marked periods longer than 1 h with

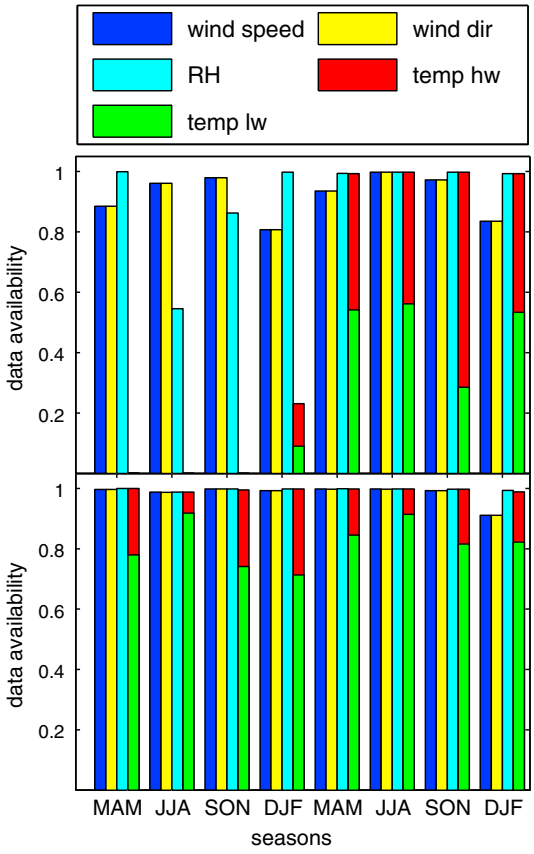

Figure 3. Seasonal data availability from the (top) Ulriken and (bottom) GFI AMS. The temperature data are divided into measurements during high wind speeds above 5 m/s (temp hw) and below that (temp lw).

0 m/s wind speed or constant wind direction as icing events and removed such data. To account for residual snow or ice we also removed all wind data within 30 min after icing events.

The wind distribution at Ulriken and the GFI are not representative of the free atmosphere or the ABL at the top of the valley due to various local effects on the wind field, such as speedup, blocking, and channeling [*Jonassen et al*., 2012]. Upper air observations are missing in the area. Therefore, we used the European Centre for Medium-Range Weather Forecasts (ECMWF) Interim Reanalysis Data Archive (ERA-Interim) model-level wind and temperature fields at the grid point closest to Bergen (0.25° interpolated grid) for the description of the synoptic situation. Analysis steps were available at 6 h resolution, and prediction steps were available at 3 h resolution beginning a new prediction once every 12 h. To reach a 3 h resolution with the highest available quality, we combined analysis steps with prediction steps always using the shortest possible lead time.

For the comparison of the pollution events to the meteorological conditions, we used hourly averaged measurements of the concentrations of NO_2 (μ_{NO_2}), $PM_{2.5}$ $(\mu_{PM_{2.5}})$, and PM_{10} $(\mu_{PM_{10}})$ from a reference station for the pollution in proximity to dense traffic. The station is located at Danmarksplassen, approximately 1000 m southeast from the GFI on the opposite side of the sea inlet. This station measures the air quality at one of the busiest traffic junctions in the city. The area around this location is also densely populated and considered of central importance for future city development. The data are available from the Norwegian Institute for Air Research (NILU) at http://admin.luftkvalitet.info.

2.4. Separation of Temperature Gradients

The linear temperature gradient across the layer i to $i+1$, where z_i is the central height ascribed to the temperature at the level i in the MTP-5HE data, is obtained as

$$\Delta T_i = (T_{i+1} - T_i)/(z_{i+1} - z_i)$$

Here $i \in \{1, \ldots, 20\}$, $z_{i+1} - z_i = 50$ m, $z_1 = 45$ m, and $z_{i+1} = z_1 + 50\ \text{m} \cdot (i-1)$. From this we identified temperature profiles containing inversions defined as $\Delta T_i > 0$ K for at least one of $i \in \{1, \ldots, 20\}$. An investigation of the profiles containing temperature inversions showed that there were two different types of inversions not necessarily connected to each other: ground-based temperature inversions (G-inversions), defined as temperature profiles with $\Delta T_1 > 0$ K and elevated temperature inversions (E-inversions) defined as profiles with $\Delta T_i > 0$ K for at least one $i \in \{2, \ldots, 20\}$ and $\Delta T_1 \leq 0$ K. Taking advantage of the high temporal resolution of the MTP-5HE measurements we developed a method to automatically identify the inversion type. It is hereby important to eliminate the cases with unclear inversion type, e.g., when E-inversions resulted from breaking G-inversions when a mixing layer starts to appear in the lowest part of the inversions as observed by *Berge and Hassel* [1984]. This is not given by a simple separation into ground-touching and not ground-touching inversions as it has, for example, been used by *Miller et al*. [2013].

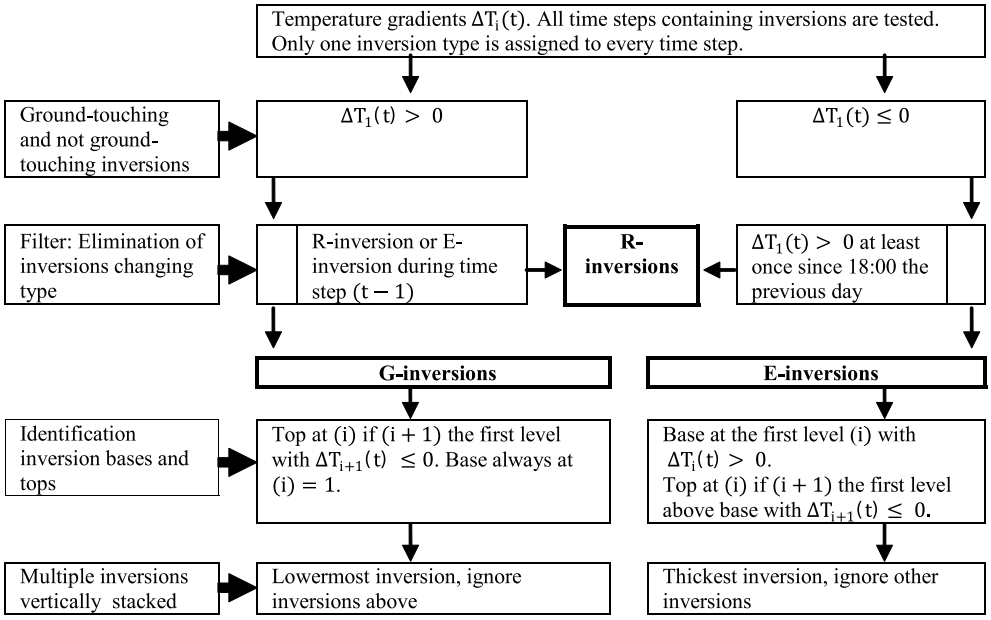

Figure 4. Identification scheme for the inversion types. All temperature differences are given in K.

The scheme for the identification of the inversion type is shown in Figure 4. In a first step we identified all measurements containing any temperature inversions. We then assigned each of these profiles to one of the three classes G-inversions, E-inversions, or R-inversions—residual inversions that could not be identified as one of the other two classes. This study focuses exclusively on the G-inversions and E-inversions. The separation is based on the location where the inversion signal first appeared. G-inversions start growing from the ground upward, whereas E-inversions first appear at an elevated position. G-inversions are the much more frequent inversion type in the Bergen valley. In order to remove the G-inversions that were breaking up by the formation of a mixed layer from the ground, we only defined inversions as E-inversions if there were no measurements with inversions right above the ground ($\Delta T_1 > 0$ K) since the last evening (18:00 UTC). For G-inversions, we used a less strict condition that the inversion signal first had to appear from the ground.

We then combined successive profiles with the same inversion type to inversion episodes similar to *Liou and Yan* [2006] before we finally identified the key features of both the single inversions and the inversion episodes based on the following definitions: If the temperature inversion is found between levels i_b and i_{t+1} where $i_b < i_{t+1}$, then the heights of the inversion base and the inversion top are defined correspondingly as

$$z_{\text{base}} = (z_{i_b} + z_{i_b+1})/2 \text{ and } z_{\text{top}} = (z_{i_t} + z_{i_t+1})/2$$

The inversion thickness and strength are defined as

$$\Delta z = z_{i_{t+1}} - z_{i_b} - z_{\text{base}} \text{ and } \Delta T_{\text{total}} = T_{i_{t+1}} - T_{i_b}$$

It is clear that the decrease in effective vertical resolution with height puts some constraints on the accuracy of the identified inversion features. That is a general drawback of microwave remote sensing data.

3. Results and Discussion

Generally, G-inversions appear in synoptic situations with a strongly negative surface heat balance in the valley, whereas the atmospheric layers above the valley are relatively free to mix even though they are also often stably stratified. E-inversions appear in situations when the ground layers are better mixed than the layers aloft. This can, for example, be caused by elevated warm air advection decoupled from the surface processes or subsidence. In this chapter we discuss the properties of the G-inversions and E- inversions. We also analyze the statistical link between G-inversions and E- inversions and cases of high pollution with NO_2 or PM.

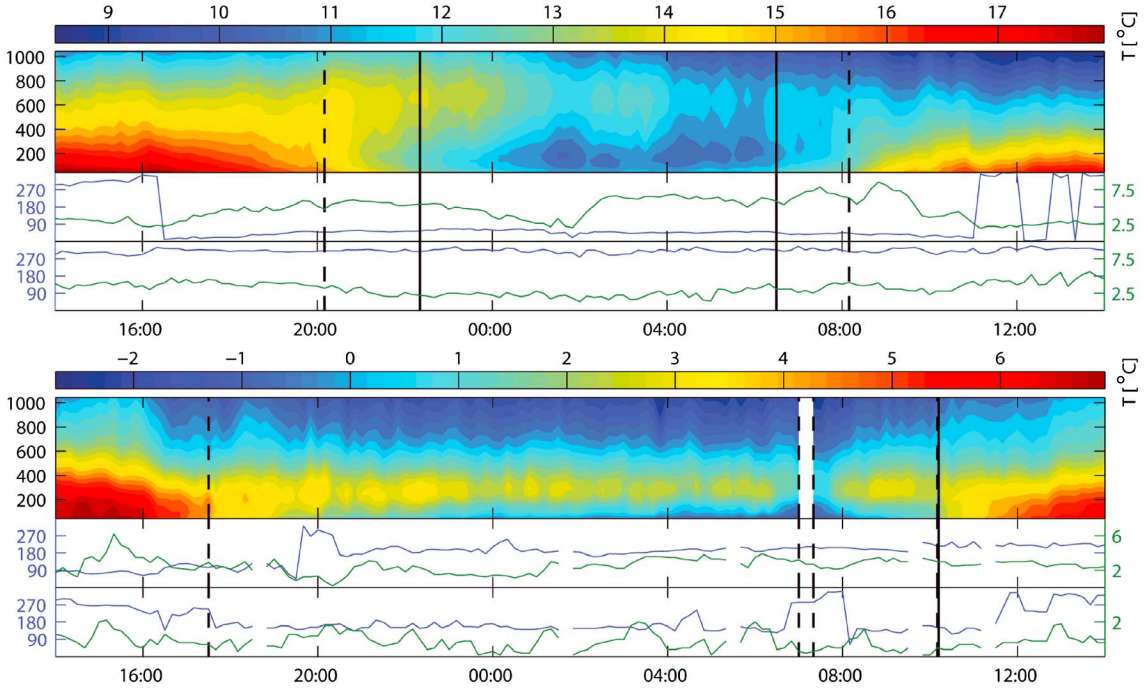

Figure 5. Example of an E-inversion (between 14 and 15 July 2011, top) and a G-inversion (between 24 and 25 February 2013, bottom). The contour plots show the MTP-5HE-measured temperature profiles (*x* axis units (time) in UTC, *y* axis units (m asl)). The line plots show the wind directions in degrees (blue) and speeds in m/s (green) at the Ulriken and GFI AMS. The dashed lines show the beginning and start of the inversion episodes. The solid lines show sunrise and sunset. Sunset during 24 February occurred at 13:50 UTC. The G-inversion contains a data gap of 10 min.

3.1. Case Study of G-Inversion and E-Inversion

The following case study illustrates the evolution of these two types of temperature inversions as observed with the MPT5-HE. The characteristics of a G-inversion (24 to 25 February 2013) are exemplified in Figure 5 (bottom). The surface pressure at the GFI AMS rose from 1023 hPa in the afternoon of 24 February to 1032 hPa throughout 25 February, indicating anticyclonic synoptic weather conditions. The sky was free from clouds (cloud observations from surface synoptic observations downloaded from www.eklima.no). The wind speed was less than 2 m/s at the GFI and 5 m/s at the Ulriken AMS. The ground was snow free, and the large sea inlet close to the GFI was free from ice. As predicted by the atmospheric radiation [e.g., *Niemela et al.*, 2001] and ABL [*Zilitinkevich and Esau*, 2007] models, the surface temperature initially dropped faster than the temperature of the mixed layers due to the positive feedback between the surface cooling and suppression of near-surface turbulent mixing.

The inversion top was at 220 m asl, which is within the valley, while the air at the mountain tops around remained less strongly stratified. This was probably linked to the existence of a separated boundary layer over the mountains. In this case, the mean wind would be oriented approximately along the valley axis at all levels within the inversion, making the MTP-5HE and the GFI AMS measurements representative for the entire valley except for large stagnation zones caused by the curvature of the valley and the topography on the base of the valley.

The mean inversion strength was 2.2 K. At this temperature difference, the radiation restratification processes and the turbulent mixing compensated each other. Because of the turbulent mixing the theoretical radiative equilibrium level of about 2 km height [*Overland and Guest*, 1991] was never reached—we never observed G-inversions extending beyond 970 m asl.

The data also show that the G-inversion was not destroyed by increasing winds but instead might have been destroyed by the increasing surface heating that finally warmed the lower air layers to temperatures above the maximum temperature of the inversion. The exact mechanisms of the inversion breakup are still debatable.

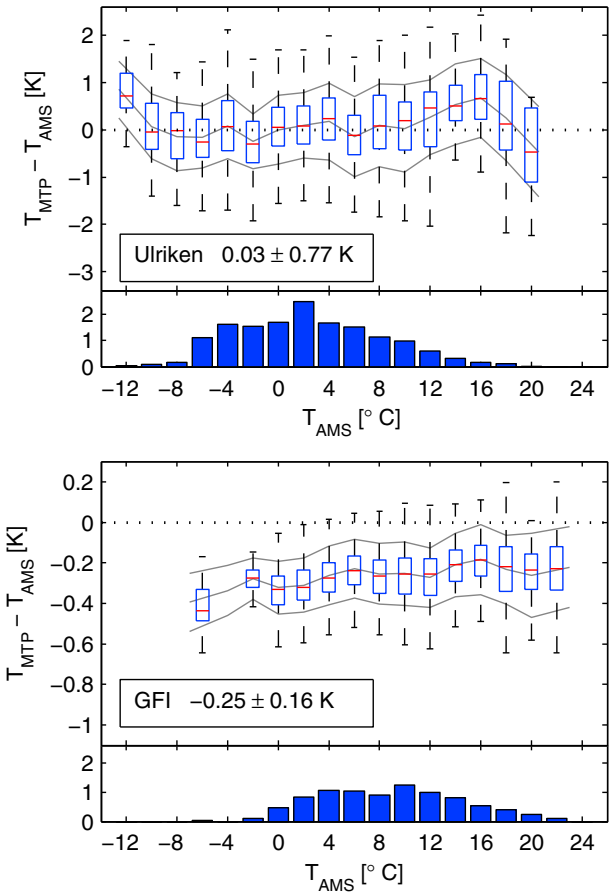

Figure 6. Intercomparison of temperatures at the AMS and MTP-5HE at the heights of the AMS for (top) Ulriken and (bottom) the GFI. The box and whiskers plots show the statistics of the temperature difference between the MTP-5HE and the AMS; bar graphs show the histograms of temperature measurements at the AMS (number of measurements divided by 1000). Only measurements with wind speeds in excess of 5 m/s at the respective AMS are used. The boxes show the median and the 25 and 75 percentiles. The maximum whiskers lengths are the 1.5 interquartile ranges. The grey lines show the mean and RMS differences.

The E-inversion occurred during the night from 14 to 15 July 2011 (Figure 5, top). The sky was almost cloud free during 14 July and became overcast during the night. The air pressure at the GFI AMS fell from 1010 hPa at 14:00 UTC, 14 July to 1004 hPa at 14:00 UTC the next day. The wind speeds were below 7.5 m/s at Ulriken and below 5 m/s at the GFI. At the same time, ERA-Interim showed weaker winds with a maximum wind speed of 4.8 m/s at 450 m asl during 14 July 21:00 UTC. The Ulriken AMS wind measurements suggest a northeasterly flow across the valley. The advected air had relatively high temperatures so that the dense cooler air was trapped in the valley. The wind direction at the bottom of the valley was rotated by 90° relative to the free flow direction, as it should be expected when the valley recirculation is forced.

The E-inversion could be interpreted as penetration of the upper air into the valley at the top of a recirculation eddy. *Mohamad and Viskanta* [1995] showed that a cross-valley flow under stable stratification is strongly dependent on a combination of buoyancy and inertia forces as well as on the position of measurements relative to the recirculation eddy. If this also applies to E-inversions created by the westerly cross-valley flows, they could be severely underrepresented in our data set as their recirculation eddies would be shifted aside from the direction of the MTP-5HE line of view.

This particular E-inversion existed in the layer between 220 m asl and 570 m asl, resulting in a mean inversion thickness of 365 m. The mean inversion strength was 0.97 K. The inversion was descending throughout the night. Like the ground inversion, the elevated inversion was most likely broken down by a developing convective state of the ABL after sunrise.

3.2. Intercomparison of the MTP-5HE With Automatic Meteorological Stations

We used the temperature measurements from the same two AMS that we already used for the MTP-5HE data filtering for an intercomparison with the MTP-5HE measured temperatures at the same heights as the AMS. This gave us an estimation of the reliability of the MTP-5HE measured profiles since radio soundings are not possible in the Bergen valley. Intercomparisons of MTP-5HE and similar instruments to radiosondes have been conducted before and the results are summarized in section 2.2.

The MTP-5HE measurements require a different meteorological interpretation compared to the in situ measurements at the AMS. We expect that the largest differences are caused by the decreasing vertical resolution of the instrument and the overlapping weighting functions applied to the single angular measurements in the inversion algorithm [*Snider*, 1972]. This should lead to a smoothing of the profiles measured with the MTP-5HE especially under complex vertical temperature structures like sharp E-inversions. Furthermore, we expect differences between the free valley ABL temperature, which is measured with the

Table 1. Intercomparison of MTP-5HE and Ulriken AMS[a]

	Inversion Free	G-Inversions	E-Inversions
Mean difference (K)	0.03 (0.77)	0.10 (0.70)	−0.66 (0.53)
Number profiles	4750	1323	86

[a]Mean (standard deviations) for the differences between the Ulriken AMS and MTP-5HE for measurements from March 2012 to February 2013.

MTP-5HE, and the local meteorological conditions at the elevated AMS, which is affected by proximity to the surface [*Fitje*, 1972; *Kirchner et al*., 2013] especially during situations with low wind-induced mixing.

Our intercomparison revealed that the temperature differences between the Ulriken AMS and the MTP-5HE measured temperatures at the same height were indeed high during conditions with low wind speeds. Correspondingly, we only considered cases when the wind speed exceeded 5 m/s at the Ulriken AMS for comparison. For consistency, we repeated the same for the GFI AMS. The results of the intercomparison are shown in Figure 6. At the GFI, differences were generally small with a negative bias between −0.4 and −0.2 K. Ulriken shows no overall bias but a distinctly increased root-mean-square (RMS) variation of the temperature differences. The differences were largest during very low temperatures below around −10°C and at high temperatures around 16°C. The reason for this is unknown but could also be an artifact of the few measurements under such conditions.

The temperature differences between the MTP-5HE and Ulriken AMS separated into profiles with the two inversion types and profiles without inversions are shown in Table 1. The mean differences were small during inversion-free conditions and G-inversions but substantially larger during E-inversion. This anomaly is consistent with the suggested mechanism controlling the E-inversions through the cross-valley recirculation. We assume that G-inversions are associated with stably stratified but homogeneous conditions across the valley, whereas the conditions during the E-inversions are more heterogeneous as the recirculation pushes the cold air mass toward one side of the valley. At the same time, this also fits the expectations of a decreased reliability of the MTP-5HE data in such conditions, as reported by *Kadygrov et al*. [2001]. The larger RMS during inversion-free conditions was most likely caused by the diversity of atmospheric conditions in this stability class.

3.3. Temperature Profiles in the Lowest 1000 m of the Atmosphere

In the Bergen maritime climate, the seasonal cycle is not very pronounced. Therefore, shorter synoptic variability considerably modifies the stability conditions, resulting in significant climatological anomalies on the yearly and even decadal basis. Stability is particularly sensitive to the number and persistence of wintertime anticyclonic events, often referred to as atmospheric blockings. The winter of 2012/2013 contained many more cases with strongly stable stratification of the lowest 1000 m than the winter of 2011/2012. This is clearly visible in the averaged seasonal temperature profiles and vertical temperature gradients in Figure 7. The other seasons show no significant year-to-year differences, as the unstable situations are rather similar and mainly determined by the sea surface temperature. The seasonally averaged temperatures from the AMS are given in Table 2. The AMS and MTP-5HE temperature structures are rather similar, increasing our confidence that the more frequent MTP-5HE data gaps

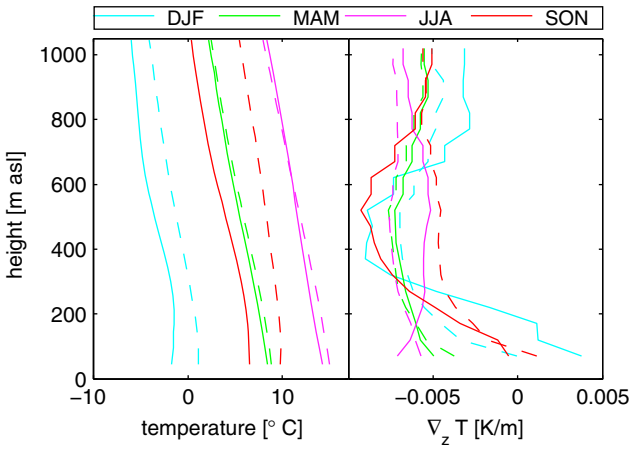

Figure 7. (left) Mean seasonal MTP-5HE temperature profiles and (right) temperature gradients. Dashed lines show the profiles from spring 2011 to winter 2011/2012, full lines from spring 2012 to winter 2012/2013.

Table 2. Temperatures at the GFI AMS[a]

Season	MAM	JJA	SON	DJF	MAM	JJA	SON	DJF
GFI AMS	7.4 (4.5)	14.1 (2.8)	10.4 (3.4)	3.0 (2.7)	7.0 (4.4)	13.7 (3.2)	7.8 (3.4)	0.5 (4.5)
MetNo	7.8 (4.7)	14.7 (3.1)	10.4 (3.7)	3.0 (2.9)	7.4 (4.7)	14.3 (3.5)	7.9 (3.7)	0.2 (4.3)
Ten year MetNo	7.4 (0.8)	15.1 (0.8)	8.8 (1.2)	2.1 (1.8)				

[a]Seasonal mean (standard deviations) temperatures in °C for the GFI AMS and the measurement site of the Norwegian meteorological institute (MetNo) in front of the GFI (25 m below the GFI AMS) from March 2011 to February 2013. The last row shows the 10 year mean seasonal temperatures from MetNo.

due to the often poor conditions for microwave radiometer operation did not bias the temperature data set considerably.

The 2 year MTP-5HE record of the atmospheric stability expressed as the vertical temperature gradient in the Bergen valley is shown in Figure 8 (left). We identified three typical stability layers. The lowermost layer (0 m asl–300 m asl) consists of the air mass trapped in the valley between the lateral ridges. It is characterized by the monotonic decrease of stability with elevation, a strong skewness of the vertical temperature gradient distribution, and a large number of strong temperature gradients up to 0.03 K/m. Figure 8 (right) reveals that this skewness and stability anomalies should be attributed to the frequent development of G-inversions. The number of E-inversions and R-inversions is rather small in this layer. The middle layer (300 m asl–700 m asl) consists of the partially free air mass that is disturbed by the mountain ridges on the one side and the large plateau on the other side of the valley (Figure 1). It is characterized by the low skewness in the distribution of temperature gradient anomalies. On average, this layer is better mixed than the free atmosphere above (the upper layer above 700 m asl) and might be the nighttime residual layer of the well-mixed daytime ABL. Some additional mixing might be connected to perturbations downwind from the plateau. The horizontal atmospheric advection is partially penetrating in this layer causing the E-inversions which are observed here to be as frequent as the thick G-inversions that reach these levels. The upper layer is the lower part of the free atmosphere, which is not considered in this study. Large mean and median temperature gradients at 670 m asl and above might indicate the prevailing height of the top of the SBL.

3.4. G-Inversions

Temperature inversions are only the most extreme cases of the more frequently observed stably stratified ABL. These extreme cases are challenging for remote sensing inversion algorithms but important for meteorological applications. As we already presented, the MTP-5HE correctly measures the temperature at elevated positions, even in the most stably stratified cases. This gives us the opportunity to study a 2 year record of temperature inversions inaccessible with other instruments. Figure 8 (right) shows that the total number of registered temperature inversions in Bergen is rather high. Most of these inversions are G-inversions. A large portion of the

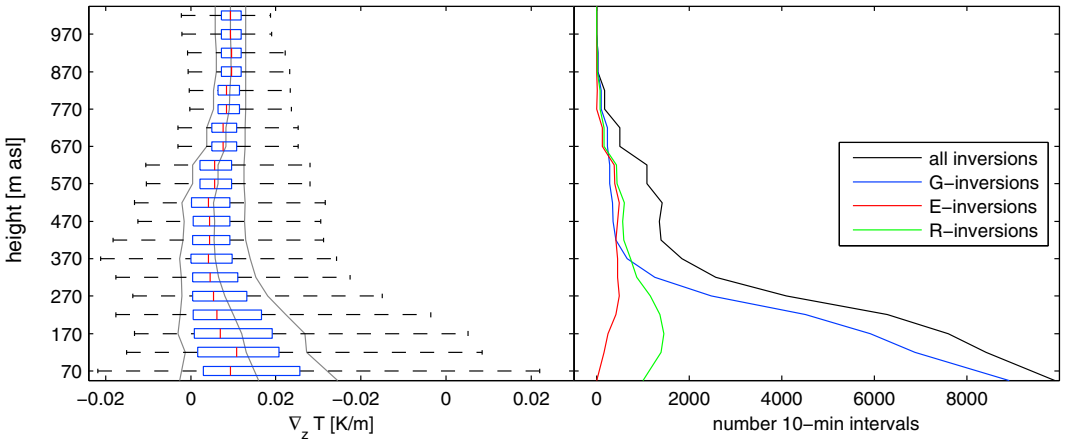

Figure 8. (left) MTP-5HE temperature gradients and (right) total occurrence of inversions, including the result of the separation into G-inversions and E-inversions. The boxes show the median and the 25 and 75 percentiles. The maximum whiskers lengths are the 2.5 interquartile ranges. The grey lines show the mean and RMS values.

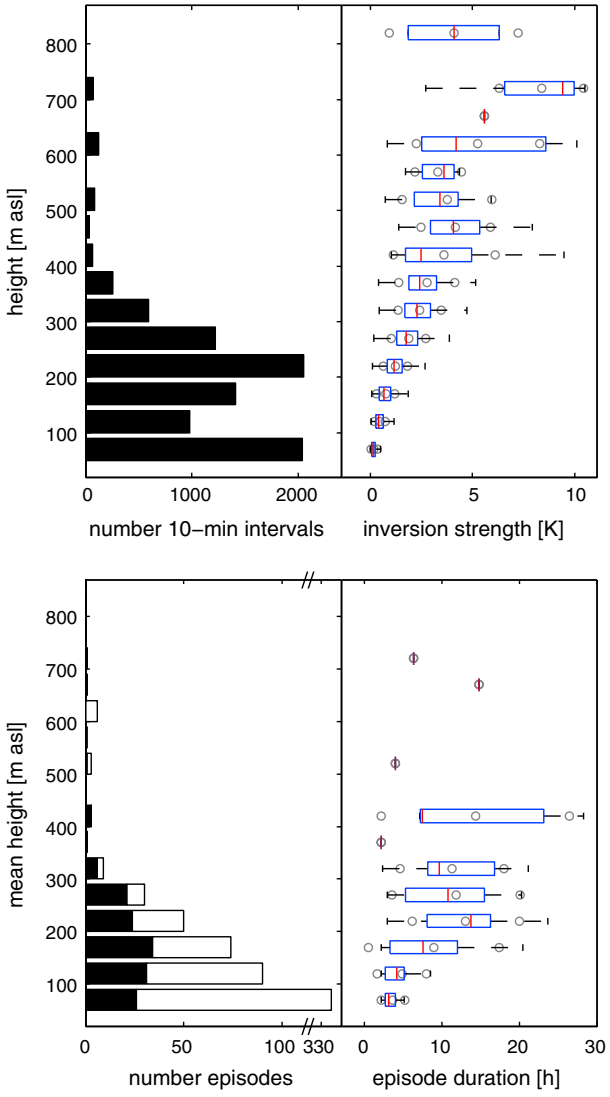

Figure 9. (top and bottom left) Inversion top against the number of G-inversion profiles and inversion episodes, (top right) inversion top against inversion strength of G-inversion profiles, and (bottom right) mean top against duration of G-inversion episodes. The number of G-inversion episodes (Figure 9, bottom left) is separated into episodes lasting shorter than 2 h (white) and longer (black). The duration of inversion episodes (Figure 9, bottom right) is only shown for inversions lasting longer than 2 h. The boxes show the median and the 25 and 75 percentiles. The maximum whiskers lengths are the 1.5 interquartile ranges. The grey circles show the mean and RMS values. The *x* axis in Figure 9 (bottom left) is broken.

G-inversions are shallow, with 30% of them thinner than 100 m. The number of vertically extended G-inversions occupying the entire valley depth was less than 500. They occurred less frequent than the E-inversions. E-inversions occurred most frequently between 420 and 620 m asl.

The vertical structure of the G-inversions is presented in Figure 9. The tops of the G-inversions were most frequently located at about 70 m asl. A second, previously unidentified maximum of the G-inversion tops existed at 220 m asl. The mean strength of the G-inversions increases up to 470 m asl. We found that most of the shallow G-inversions were only lasting a few tens of minutes, suggesting that airflow perturbations destroyed the strongly stable stratification. Therefore, we considered persistent G-inversions lasting longer than 2 h separately. Their mean tops are nearly uniformly distributed up to 270 m asl with a maximum at around 170 m asl. The mean duration of such persistent inversions is 13.1 h. The height of their mean tops was around 220 m asl. The abrupt decrease of the number of inversion episodes with mean tops above 270 m asl might be connected to the local mountain shelter effect [*Jonassen et al.*, 2013]. A few G-inversion episodes coincided with large-scale warm air advection, leading to unusually deep and strong G-inversions where the inversion tops reached levels of above 470 m asl. Those episodes are rare; only four events occurred over the 2 year period under investigation.

As expected, the remaining G-inversions are most frequent during nighttime and in the winter months (Figure 10). It is easy to observe that as the nights grow longer, the duration and strength of the G-inversions increase as well. More than 60% of the valid measurements between 18:00 and 8:00 UTC, December 2012 to February 2013 showed inversions. Again, the differences between the winter of 2011/2012 and the winter of 2012/2013 are visible with much less and weaker inversions in the first year.

3.5. E-Inversions

Compared to the G-inversions, E-inversions are in general less frequent. The tops of E-inversions revealed two maxima in the frequency distribution, at about 270 m asl and 620 m asl (Figure 11, left). Similarly, there are also two spikes in the thickness distribution. The base of the E-inversions was mostly located below 270 m asl. This level is close to the height of the G-inversion tops and marks the upper boundary of the air mass trapped

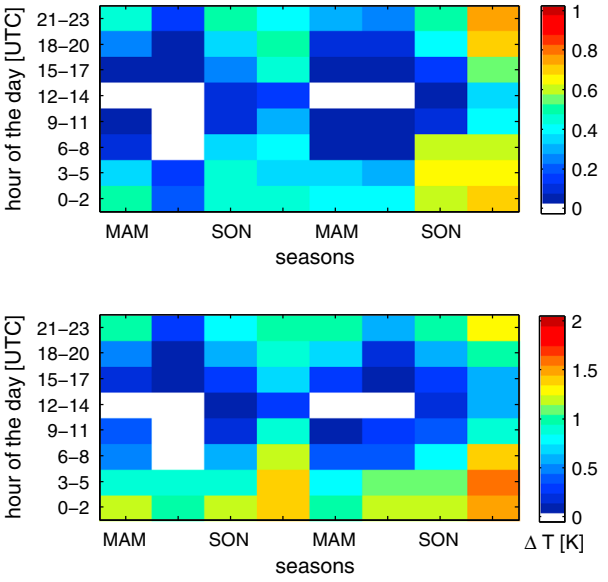

Figure 10. Diurnal and annual average fraction of time intervals with G-inversions based on the (top) quality-controlled data and (bottom) mean G-inversion strength. All data are binned as 3 monthly and 3-hourly. Blank spots indicate the occurrence of no inversions. Sunrise and sunset with the real horizon seen from the GFI are usually around 06:00 and 14:00 UTC during 15 October and around 09:30 and 12:30 UTC 15 during January. These times are very different for different parts of the valley. The minimum and maximum sun times at the GFI are around 09:30–11:30 UTC and 04:15–20:30 UTC during December and 21 June.

in the valley. This observation further supports our attribution of E-inversions to advective processes in contrast to the local radiative processes responsible for the G-inversions.

The strength and vertical extension of the E-inversions are well correlated. The maximum E-inversion duration is low (12.2 h) for 350 m thick inversions. In 43 of the 70 elevated inversion episodes between March 2011 and February 2013 the time between two adjacent episodes was less than 24 h, indicating that the conditions favoring elevated inversions persisted over longer periods. Figure 12 revealed that the diurnal and seasonal patterns of E-inversions do not follow the patterns of the G-inversions. The E-inversions occurred mostly during the warm months and late at night. The duration of the inversions in the summer seasons is limited by the long summer days with strong solar heating that mixes the ABL and erodes away the stable stratification. The total length of inversion episodes might be underrepresented because of some short-lasting data gaps in the MTP-5HE data set such as in the G-inversion case study presented in Figure 5.

E-inversions often coincided with clouds at the Ulriken AMS. When including measurements with RH at the Ulriken AMS above 95% into the analysis, the total number of 10 min averaged measurements changed from 36,004 to 64,104. The number of measurements with G-inversions only changed from 8917 to 12,119, meaning that most of the G-inversions occurred during cloud-free conditions. The number of measurements

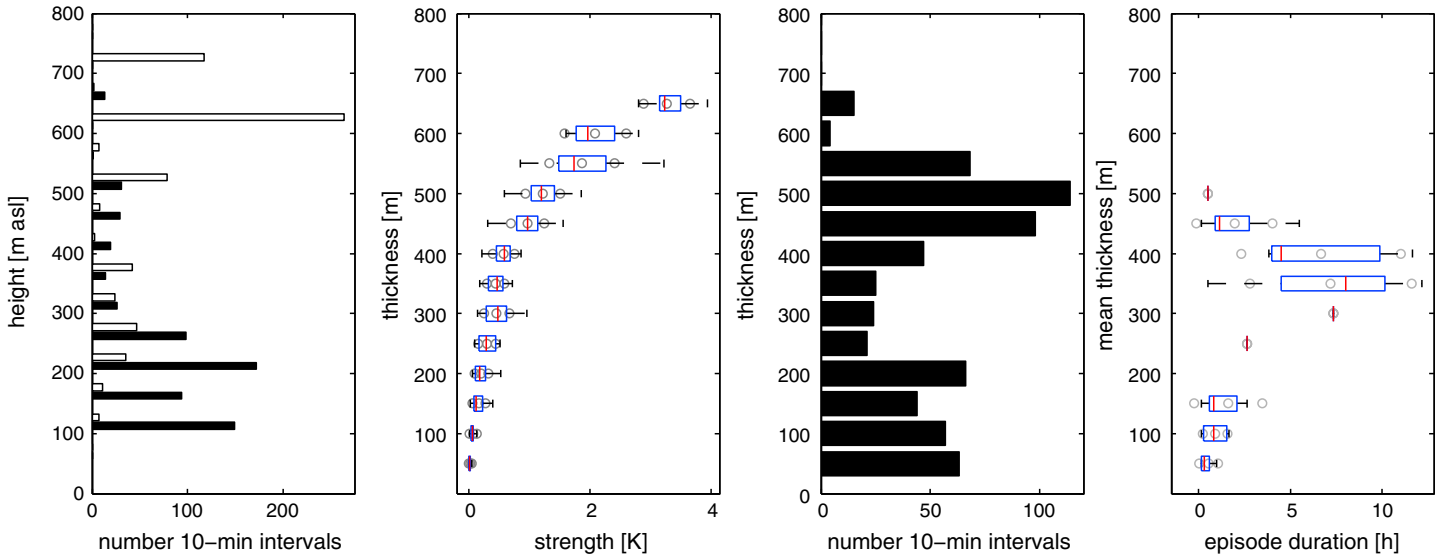

Figure 11. Inversion top (white) and base (black) against (first panel) number of E-inversion profiles, (second panel) inversion thickness against inversion strength of E-inversions, (third panel) thickness of E-inversions, and (fourth panel) mean thickness against duration of E-inversion episodes. The boxplots show the median and the 25 and 75 percentiles. The maximum whiskers lengths are the 1.5 interquartile ranges. The grey circles show the mean and RMS values.

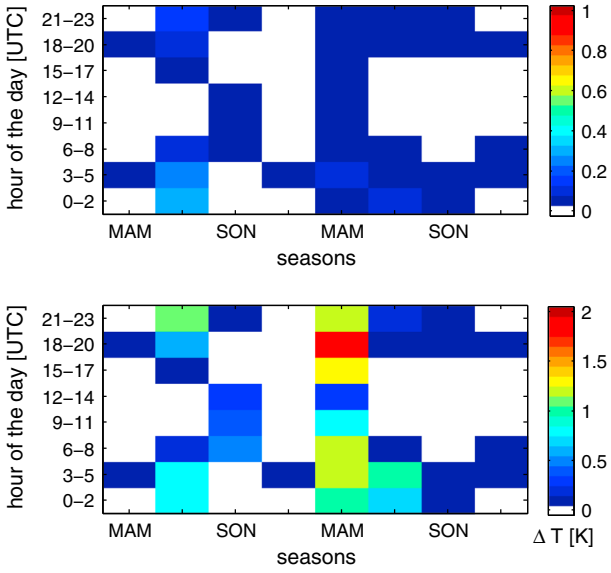

Figure 12. Fraction of time intervals with E-inversions and inversion strength of E-inversions (for details see caption Figure 10).

with E-inversions on the other hand changed from 646 to 1518. If we neglect any filtering, the number of G-inversions did not change significantly, while the number of E-inversions changed even stronger from 646 to 4395. This, however, might also include more E-inversions caused by frontal systems.

3.6. Attribution of Temperature Inversions in the Context of Flow Conditions Above the Valley

We already mentioned that the temperature structure within and above the valley is determined by the interplay between the local radiative forcing and the stability of the large-scale atmospheric flow determined by the horizontal advection. Such interplay was studied in a number of works [e.g., *Hoch et al*., 2011; *Esau and Repina*, 2012; *Katurji and Zhong*, 2012; *Ritter et al*., 2013] but only the high-frequency data acquired with the MTP-5HE instrument allows for the study of systematic differences associated with the observed temperature structure.

Figure 13 shows the meteorological wind roses at the bottom of the valley (GFI), the top of the lateral mountain ridges (Ulriken), and in the free atmosphere over Bergen (ECMWF). The wind roses for all weather conditions at the GFI and Ulriken are similar to the wind roses for the area presented by *Valved* [2012]. The ERA-Interim wind distribution found by *Jonassen et al*. [2012] is different from the wind distribution for all weather conditions because of our choice of presenting the wind distribution at around 650 m asl instead of the more widely used 850 hPa level, which corresponds to around 1 500 m asl. This choice is connected to the wind distribution during E-inversions and explained in more detail below. The AMS at the GFI shows a clear influence of channeling in the valley.

The wind roses corresponding to the G-inversions and E-inversions are drastically different. The G-inversions are characterized by southeasterly ground-level winds aligned with the major axis of the valley. At the Ulriken AMS, the G-inversion wind rose is similar to that of the all weather conditions if only considering low wind speeds. The ERA-Interim wind rose is characterized by the absence of the northwesterly wind sector, corresponding to winds advected from the Atlantic Ocean, and has a distinct southeasterly tail. The latter indicates the existence of a wake downwind of Mount Ulriken, allowing G-inversions to exist even under wind speeds as high as 16 m/s from this direction. We considered an ERA-Interim output step as coinciding with an inversion if an inversion has been measured with the MTP-5HE somewhere between the 30 min prior and 30 min after the output step.

The E-inversions are characterized by the rarely occurring northwesterly ground-level winds and northeasterly winds at the mountain top. This shows that the E-inversions are by nature linked to specific large-scale synoptic conditions. The distribution of wind directions in ERA-Interim during E-inversions was similar from the lowest model level up to model level 7, which is centered at around 650 m asl with the model topography at 258 m asl. The distribution of wind directions quickly became noncoherent above that. This shows that the more widely used 850 hPa winds are not a good indicator for the identification of E-inversions when using ERA-Interim model results.

It is to some degree surprising that the wind roses do not reflect the bimodal distribution of the inversion top levels and vertical extension. We suspect that this bimodal distribution of the mean inversion thicknesses is not an effect of different wind distributions but rather an effect of the persistence and strength of the inversions with the thicker inversions lasting longer than the thinner ones, as it might be expected from fluid mechanics studies [*Mohamad and Viskanta*, 1995].

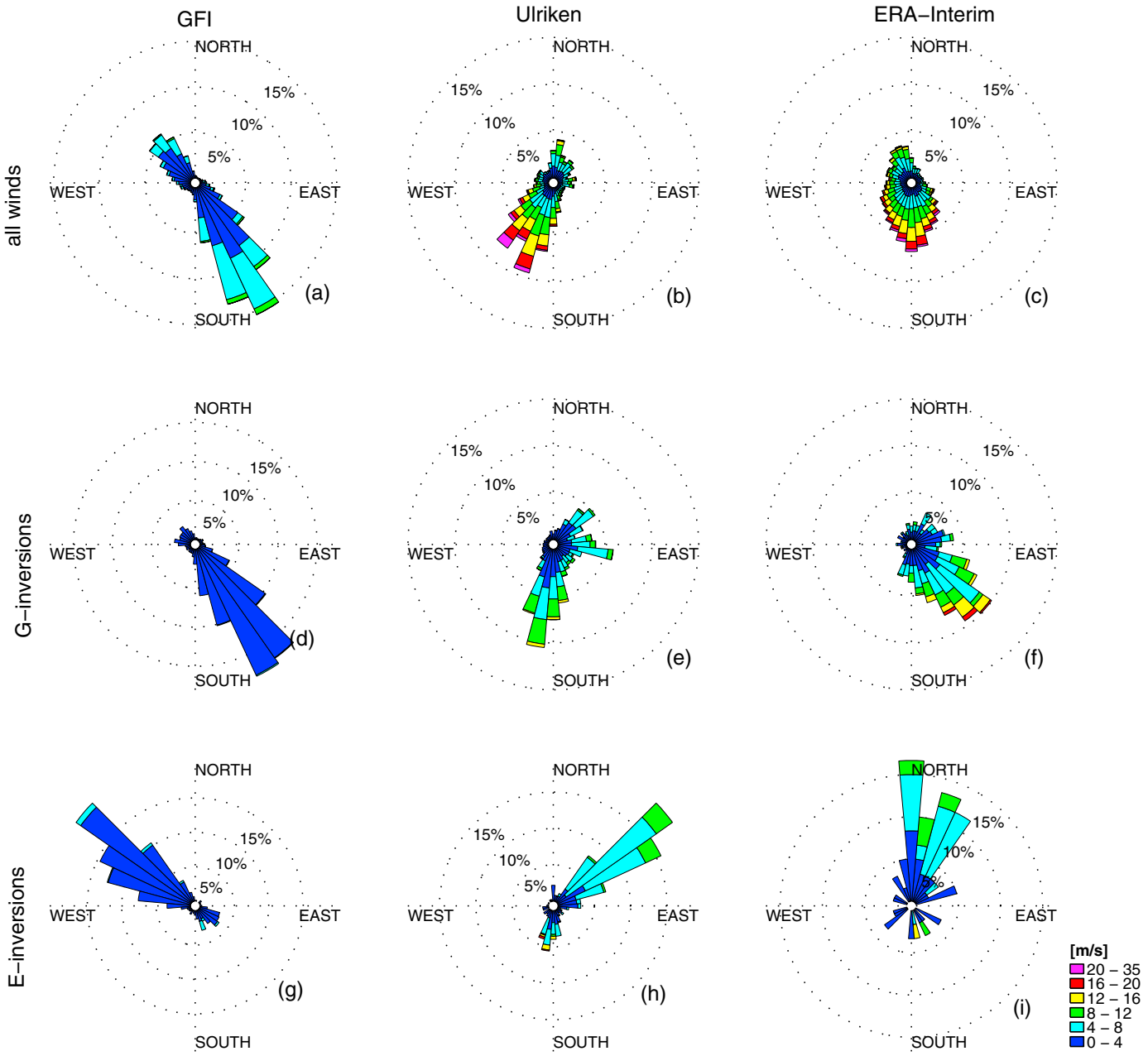

Figure 13. (a, d, g) Wind distributions at the GFI AMS and (b, e, h) the Ulriken AMS and (c, f, i) ECMWF ERA-Interim model results at model level 7, centered at 395 ± 6 m above ground level with ground level at 258 m asl during all weather conditions (Figures 13a–13c), G-inversions (Figures 13d–13f), and E-inversions (Figures 13g–13i). The common color bar is shown in the lower right corner. Percentage rings at 5, 10, and 15% indicate the fraction of the total valid data in each sector.

An interesting questions is whether the ERA-Interim reanalysis adequately represents the observed temperature inversions and furthermore the intended physical mechanisms of their development. Up to date climatological studies of the temperature inversions in the climate models and reanalysis were limited to comparisons with satellite and radio sounding data of poor vertical or temporal resolution [e.g., *Medeiros et al.*, 2011]. We found 624 ERA-Interim output steps to coincide with G-inversions, and 53% of these also showed an inversion between the lowermost two model levels in ERA-Interim that were on average centered at 9.7 m and 33.9 m above ground. For E-inversions, 60 ERA-Interim output steps coincided with inversions and 32% of these also showed elevated inversions in ERA-Interim. In addition, 58% of the measured E-inversions coincided with inversions between the lowermost two model levels in ERA-Interim. Overall, 1469 and 1100 ERA-Interim output steps showed inversions between the lowest model levels and only elevated

Table 3. Association of Temperature Inversions to Pollutant Concentrations for the Measurement Station Danmarksplassen[a]

	Low	Moderate	High	Very High
NO_2 concentration interval ($\mu g/m^3$)	0–100	100–150	150–200	200–250
Measurements	15,942	885	159	22
All inversions	1,071 (1,718)	286 (400)	99 (139)	17 (20)
G-inversions	776 (1,289)	245 (358)	92 (133)	17 (20)
E-inversions	70 (151)	1 (3)	0 (0)	0 (0)
No data	11,404	354	23	1
$PM_{2.5}$ concentration interval ($\mu g/m^3$)	0–25	25–50	50–100	100–125
Measurements	16,555	561	135	3
All inversions	1,044 (1,733)	305 (400)	104 (121)	3 (3)
G-inversions	733 (1,281)	268 (371)	103 (121)	3 (3)
E-inversions	71 (154)	0 (0)	0 (0)	0 (0)
No data	11,906	135	16	0
PM_{10} concentration interval ($\mu g/m^3$)	0–50	50–100	100–150	150–250
Measurements	12,445	720	96	31
All inversions	936 (1,492)	276 (380)	45 (60)	7 (14)
G-inversions	704 (1,170)	240 (345)	39 (54)	6 (14)
E-inversions	31 (89)	1 (1)	0 (0)	0 (0)
No data	8,713	194	13	6

[a]Given are the total numbers of hourly pollution measurements. No data means either missing MTP-5HE data or measurements that were marked as biased. Numbers without parenthesis show the numbers of hourly pollution measurements coinciding with persistent inversions lasting longer than 2 h; numbers in parenthesis describe the number of pollution measurements where an inversion was measured during at least one time step within the 1 h integration time. The difference between all inversions and the sum of G-inversions and E-inversions are R-inversions. The thresholds for the different pollution levels are chosen according to Norwegian standards (http://luftkvalitet.info).

inversions, respectively. This means that ERA-Interim significantly overestimates the total number of inversions, meaning that it seems to underestimate ABL turbulence but in addition, fails to represent a large part of the actual measured inversions. Furthermore, the inversion bases of elevated inversions in ERA-Interim were significantly too high, suggesting that this is a different type of inversions than the E-inversions within the Bergen valley.

The strong coupling of both inversion types to the local topographic features has immediate practical implication for any attempt to predict the pollutant dispersion within the valley. Such a prediction on the basis of dynamically downscaled local micrometeorological conditions with mesoscale models will only have limited success because of the too low horizontal resolution in these models.

3.7. Attribution of Pollution Measurements to the Temperature Profile

Through the reduced turbulent mixing within temperature inversions and the generally low wind speeds, ABL temperature inversions should lead to an accumulation of pollutants, especially in proximity to large local emission sources. Because of the distinct circulation that we observed during inversions it should in principle be possible to create a simple proxy that can at least represent the year-to-year statistics of meteorological conditions favorable for inversions, allowing for future projections of the pollution conditions within the central Bergen valley. Inversions by themselves, however, are not yet an indicator of high pollution events. The major pollutant sources in the Bergen valley are road traffic, wood firing, and to a lesser degree ship exhaust from the harbor. These sources have a high variability on a number of time scales requiring a careful analysis of the skill scores of such a simple proxy.

Therefore, at this point we will only focus on establishing a statistical link between high pollution events and the above described ABL temperature profiles. Table 3 shows the numbers of inversion measurements that coincided with pollution measurements within the four air pollution classes: "low," "moderate," "high," and "very high." Low pollution concentrations mostly occur during measurements without inversions—meteorological conditions with sufficient turbulence within the valley ABL. Wet deposition is a major factor in the reduction of PM concentrations. Therefore, low and moderate pollution levels often coincided with missing data at the MTP-5HE that were mostly caused by rain and clouds, often in connection with relatively high wind speeds within the valley. For high and very high pollution concentrations, only a few cases of

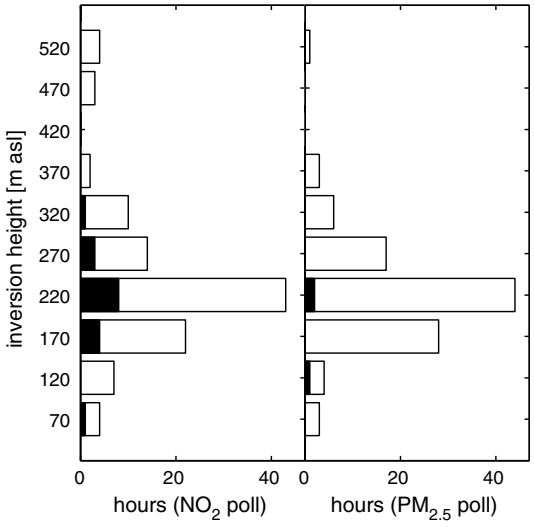

Figure 14. Inversion height of persistent G-inversions against pollutant concentration. For NO_2, the white and black bars show the number of hours with $\mu_{NO_2} > 150\ \mu g/m^3$ and $\mu_{NO_2} > 200\ \mu g/m^3$. For $PM_{2.5}$, they show the number of hours with $\mu_{PM_{2.5}} > 50\ \mu g/m^3$ and $\mu_{PM_{2.5}} > 100\ \mu g/m^3$.

missing values existed in the final, filtered MTP-5HE data set, confirming that the MTP-5HE is resolving the relevant meteorological conditions that are relevant to air pollution monitoring and prediction.

Most of the cases of high and very high pollution with NO_2 and $PM_{2.5}$ happened during persistent G-inversions (lasting longer than 2 h and extending over the entire averaging length of the air quality measurements). The measurements with very high NO_2 concentrations not coinciding with persistent G-inversions were one case of missing data because of a long-term icing event, one case with a very short G-inversion, and three cases with a residual stable layer as the result of a G-inversion during the night, two of which overlapped partially with persistent G-inversions. This also shows that our separation into nonpersistent and persistent G-inversions is adequate to remove some of the irrelevant inversions for air quality monitoring purposes. Table 3 illustrates that inversions are less relevant for pollution events with coarse particles (PM_{10}). Less than 50% of the high pollution cases coincided with inversions. In Bergen, high PM_{10} concentrations are mostly caused by road dust from studded winter tires and are not as dependent on temperature inversions as $PM_{2.5}$ and NO_2 pollution episodes.

The majority of high and very high $PM_{2.5}$ and NO_2 pollution events coincided with G-inversions that had a height between 170 and 270 m asl (Figure 14). This differs from the common perception that high pollution events coincide with either thin or unusually thick and persistent inversions. For a persistent G-inversion to be thin, the turbulence within the inversion should be extremely weak, which allows for an accumulation of pollutants in a smaller volume. But, even under the weak winds that usually exist within the valley during G-inversions, turbulence remains strong enough for the G-inversions to grow vertically until they are a few hundred meters thick.

E-inversions never coincided with high and very high pollutant concentrations, meaning that they are not relevant for air quality considerations. They are however relevant for an understanding of the general valley circulation and could be an efficient mechanism for reducing temperatures in the valley during large-scale warm air advection events.

4. Conclusions

We used long-term (2 years) continuous high-resolution measurements with the microwave temperature profiler MTP-5HE to study the structure of temperature inversions in the Bergen valley, Norway. This region, with its temperate maritime climate, is typical for the high-latitude coastal mountain valleys where the population and economical activity are concentrated along the western coasts of Scandinavia and North America. The statistical analysis showed that temperature measurements with the MTP-5HE were overall unbiased mean difference of 0.03 ± 0.77 K during inversion-free conditions and 0.10 ± 0.70 K during ground-based temperature inversions—compared to measurements with an elevated mountain AMS with some restrictions on the meteorological conditions.

The temperature profiles revealed two distinct types of temperature inversions trapped in the valley, namely, ground-based G-inversions and elevated E-inversions, which cannot be adequately described with a network of mountain meteorological stations. We described their properties (inversion height, thickness, and strength) and under which conditions the inversions exist. This analysis demonstrated that the G-inversions and E-inversions are caused by distinctly different physical mechanisms. The existence of G-inversions is very common during winter nighttime. During winter nighttime 2012/2013 more than 60% of all measurements, taken during favorable meteorological conditions for the operation of the MTP-5HE, showed this type of

inversion. Because the valley is protected by the local topographic features they can exist during a wide range of synoptic scale wind speeds. E-inversions only occur during situations of unusual circulation with warm air advection directly above the valley.

The G-inversions have a strong effect on the surface layer concentration of the air pollutants. An association of pollution classes revealed that high pollution cases both with fine particulate matter and nitrogen dioxide are directly dependent on the existence of persistent G-inversions. This indicates the importance of a functioning prediction of the inversion conditions in order to provide this information to decision makers. The specific conditions under which G-inversions and E-inversions occur might give us the possibility to develop simple proxies for their prediction, allowing us to provide future projections of the pollution situation in the Bergen valley.

Our study suggests a significantly more influential role of the local topographical features than it has been previously thought and implemented into the air quality monitoring routines. Considering a minimum width of the valley base of less than 1.5 km (within which significant topographic features exist), mesoscale models with a resolution of 500 m or 1000 m that are used for today's air quality predictions are likely not sufficient. We demonstrated that both inversion types (but in particular, the E-inversions) are also poorly reproduced in ERA-Interim.

The use of microwave temperature remote sensing in the complicated conditions in the Bergen valley has been shown to be essential for practical meteorological applications like air pollution forecasts.

Acknowledgments

This study is part of the project "Bergen Air Quality under Present and Future Climate Scenarios" funded by the GC-Rieber Foundation. The MTP-5HE measurements have been provided by the Norwegian Research Council project "Planetary boundary layer feedback in the Earth's Climate System" 191516/V30. The analysis was supported by the Norwegian Centre for Climate Dynamics (SKD) project REGSCEN. The authors acknowledge Jan-Asle Olseth and Ole Edvard Grov from the Geophysical Institute of the University of Bergen for the provision of MRR and AMS data for Bergen-GFI and Ulriken. ECMWF ERA-40 data used in this study have been obtained from the ECMWF Data Server. Data from the AMS operated by MET Norway were downloaded from www.eklima.no. The pollution measurements have been provided by the Norwegian Institute for Air Research (NILU) and the Municipality of Bergen. The laser scanning data for the production of Figure 1 have been provided by the Municipality of Bergen.

References

Berge, E., and F. Hassel (1984), En undersøkelse av temperaturinversjoner og lokale drenasjestrømmer i Bergen, Meteorol. Rep. Ser., Univ. of Bergen, Bergen, Norway.

Chang, C.-M., L.-N. Chang, H.-C. Hsiao, F.-C. Lu, P.-F. Shieh, C.-N. Chen, and S.-C. Lu (2006), A further study of high air pollution episodes in Taiwan using the microwave temperature profiler (MTP-5HE), *JSME Int. J. Ser. B*, *49*(1), 60–64, doi:10.1299/jsmeb.49.60.

Esau, I., and I. Repina (2012), Wind climate in Kongsfjorden, Svalbard, and attribution of leading wind driving mechanisms through turbulence-resolving simulations, *Adv. Meteorol.*, *2012*, 1–16, doi:10.1155/2012/568454.

Esau, I. N., T. Wolf, E. A. Miller, and I. A. Repina (2013), The analysis of results of remote sensing monitoring of the temperature profile in lower atmosphere in Bergen (Norway), *Russ. Meteorol. Hydrol.*, *38*(10), 715–722, doi:10.3103/S1068373913100099.

Fay, B., and L. Neunhäuserer (2006), Evaluation of high-resolution forecasts with the non-hydrostatic numerical weather prediction model Lokalmodell for urban air pollution episodes in Helsinki, Oslo and Valencia, *Atmos. Chem. Phys.*, *6*, 2107–2128, doi:10.5194/acpd-5-8233-2005.

Fitje, A. (1972), En undersøkelse av atmosfæriske stabilitetsforhold i bergensområdet, Diploma thesis, Univ. of Bergen, Bergen, Norway.

Friedrich, K., J. K. Lundquist, M. Aitken, E. A. Kalina, and R. F. Marshall (2012), Stability and turbulence in the atmospheric boundary layer: A comparison of remote sensing and tower observations, *Geophys. Res. Lett.*, *39*, L03801, doi:10.1029/2011GL050413.

Hoch, S. W., C. D. Whiteman, and B. Mayer (2011), A systematic study of longwave radiative heating and cooling within valleys and basins using a three-dimensional radiative transfer model, *J. Appl. Meteorol. Climatol.*, *50*(12), 2473–2489, doi:10.1175/JAMC-D-11-083.1.

Ji, D., et al. (2012), Analysis of heavy pollution episodes in selected cities of northern China, *Atmos. Environ.*, *50*, 338–348, doi:10.1016/j.atmosenv.2011.11.053.

Jonassen, M. O., H. Ólafsson, J. Reuder, and J. A. Olseth (2012), Multi-scale variability of winds in the complex topography of southwestern Norway, *Tellus A*, *64*, 11962, doi:10.3402/tellusa.v64i0.11962.

Jonassen, M. O., H. Olafsson, A. S. Valved, J. Reuder, and J. A. Olseth (2013), Simulations of the Bergen orographic wind shelter, *Tellus A*, *65*, 19206, doi:10.3402/tellusa.v65i0.19206.

Kadygrov, E. N., and D. R. Pick (1998), The potential for temperature retrieval from an angular-scanning single-channel microwave radiometer and some comparisons with in situ observations, *Meteorol. Appl.*, *5*, 393–404, doi:10.1017/S1350482798001054.

Kadygrov, E. N., A. S. Viazankin, E. R. Westwater, and K. B. Widener (1999), Characteristics of the low-level temperature inversion at the north slope of Alaska on the base of microwave remote sensing data, in *Ninth ARM Science Team Meeting Proceedings*, vol. 5, U.S. Dep. of Energy, San Antonio, Tex.

Kadygrov, E. N., V. E. Kadygrov, A. D. Lykov, E. A. Miller, and A. V. Troitsky (2001), Investigation of the atmospheric boundary layer thermodynamics on the base of microwave remote sensing, in *Eleventh ARM Science Team Meeting Proceedings*, U.S. Dep. of Energy, Atlanta, Ga.

Kadygrov, E. N., M. N. Khaikin, E. A. Miller, A. Shaposhnikov, and A. V. Troitsky (2005), Advanced atmospheric boundary layer temperature profiling with MTP-5HE microwave system, in *WMO Technical Conference on Meteorological and Environmental Instruments and Methods of Observation (Teco-2005) Proceedings*, Bucharest, Romania.

Katurji, M., and S. Zhong (2012), The influence of topography and ambient stability on the characteristics of cold-air pools: A numerical investigation, *J. Appl. Meteorol. Climatol.*, *51*(10), 1740–1749, doi:10.1175/JAMC-D-11-0169.1.

Kirchner, M., T. Faus-Kessler, G. Jakobi, M. Leuchner, L. Ries, H.-E. Scheel, and P. Suppan (2013), Altitudinal temperature lapse rates in an Alpine valley: Trends and the influence of season and weather patterns, *Int. J. Climatol.*, *33*(3), 539–555, doi:10.1002/joc.3444.

Kukkonen, J., et al. (2005), Analysis and evaluation of selected local-scale PM air pollution episodes in four European cities: Helsinki, London, Milan and Oslo, *Atmos. Environ.*, *39*(15), 2759–2773, doi:10.1016/j.atmosenv.2004.09.090.

Liou, Y. A., and S. K. Yan (2006), Two-year microwave radiometric observations of low-level boundary-layer temperature inversion signatures, in *2006 IEEE International Symposium on Geoscience and Remote Sensing*, pp. 644–647, IEEE, Denver, Colo.

Loehnert, U., and O. Maier (2012), Operational profiling of temperature using ground-based microwave radiometry at Payerne: Prospects and challenges, *Atmos. Meas. Tech.*, *5*, 1121–1134, doi:10.5194/amt-5-1121-2012.

Mauritsen, T., G. Svensson, S. S. Zilitinkevich, I. Esau, L. Enger, and B. Grisogono (2007), A total turbulent energy closure model for neutrally and stably stratified atmospheric boundary layers, *J. Atmos. Sci.*, *64*(11), 4113–4126, doi:10.1175/2007JAS2294.1.

Medeiros, B., C. Deser, R. A. Tomas, and J. E. Kay (2011), Arctic inversion strength in climate models, *J. Clim.*, *24*(17), 4733–4740, doi:10.1175/2011JCLI3968.1.

Miller, N. B., D. D. Turner, R. Bennartz, M. D. Shupe, M. S. Kulie, M. P. Cadeddu, and V. P. Walden (2013), Surface-based inversions above central Greenland, *J. Geophys. Res. Atmos.*, *118*, 495–506, doi:10.1029/2012JD018867.

Mohamad, A. A., and R. Viskanta (1995), Flow and heat transfer in a lid-driven cavity filled with a stably stratified fluid, *Appl. Math. Model.*, *19*(January), 465–472, doi:10.1016/0307-904X(95)00030-N.

Niemela, S., P. Raisanen, and H. Savijarvi (2001), Comparison of surface radiative flux parameterizations. Part I: Longwave radiation, *Atmos. Res.*, *58*, 1–18, doi:10.1016/S0169-8095(01)00084-9.

Overland, J. E., and P. S. Guest (1991), The Arctic snow and air temperature budget over sea ice during winter, *J. Geophys. Res.*, *96*(C3), 4651–4662, doi:10.1029/90JC02264.

Pernigotti, D., A. M. Rossa, M. E. Ferrario, M. Sansone, and A. Benassi (2007), Influence of ABL stability on the diurnal cycle of PM10 concentration: Illustration of the potential of the new Veneto network of MW-radiometers and SODAR, *Meteorol. Zeitschrift*, *16*(5), 505–511, doi:10.1127/0941-2948/2007/0204.

Ritter, M., M. D. Müller, M.-Y. Tsai, and E. Parlow (2013), Air pollution modeling over very complex terrain: An evaluation of WRF-Chem over Switzerland for two 1-year periods, *Atmos. Res.*, *132–133*, 209–222, doi:10.1016/j.atmosres.2013.05.021.

Scanzani, F. (2010), Ground based passive microwave radiometry and temperature profiles, in *Remote Sensing for Wind Energy*, edited by A. Pena and C. B. Hasager, pp. 260–275, Technical Univ. of Denmark, DTU Wind Energy, DTU Risoe Campus, Roskilde, Denmark.

Snider, J. B. (1972), Ground-based sensing of temperature profiles from angular and multi-spectral microwave emission measurements, *J. Appl. Meteorol.*, *11*, 958–967, doi:10.1175/1520-0450(1972)011.

Troitsky, A. V., K. P. Gajkovich, V. D. Gromov, E. N. Kadygrov, and A. S. Kosov (1993), Thermal sounding of the atmospheric boundary layer in the oxygen absorption band center at 60 GHz, *IEEE Trans. Geosci. Remote Sens.*, *31*(1), 116–120, doi:10.1109/36.210451.

Trompetter, W. J., S. K. Grange, P. K. Davy, and T. Ancelet (2013), Vertical and temporal variations of black carbon in New Zealand urban areas during winter, *Atmos. Environ.*, *75*, 179–187, doi:10.1016/j.atmosenv.2013.04.036.

Valved, A. S. (2012), Local flow conditions in the Bergen valley based on observations and numerical simulations, MS thesis, Univ. of Bergen, Bergen, Norway.

Wallace, J., and P. Kanaroglou (2009), The effect of temperature inversions on ground-level nitrogen dioxide (NO_2) and fine particulate matter ($PM_{2.5}$) using temperature profiles from the Atmospheric Infrared Sounder (AIRS), *Sci. Total Environ.*, *407*(18), 5085–5095, doi:10.1016/j.scitotenv.2009.05.050.

Westwater, E. R., Y. Han, V. G. Irisov, and V. Leuskiy (1999), Remote sensing of boundary layer temperature profiles by a scanning 5-mm microwave radiometer and RASS: Comparison experiments, *J. Atmos. Oceanic Technol.*, *16*, 805–818, doi:10.1109/IGARSS.1997.609236.

Yang, S., and J. H. Christensen (2012), Arctic sea ice reduction and European cold winters in CMIP5 climate change experiments, *Geophys. Res. Lett.*, *39*, L20707, doi:10.1029/2012GL053338.

Zilitinkevich, S. S., and I. N. Esau (2005), Resistance and heat-transfer laws for stable and neutral planetary boundary layers: Old theory advanced and re-evaluated, *Q. J. R. Meteorol. Soc.*, *131*(609), 1863–1892, doi:10.1256/qj.04.143.

Zilitinkevich, S. S., and I. N. Esau (2007), Similarity theory and calculation of turbulent fluxes at the surface for the stably stratified atmospheric boundary layer, *Boundary Layer Meteorol.*, *125*(2), 193–205, doi:10.1007/s10546-007-9187-4.

Zilitinkevich, S. S., T. Elperin, N. Kleeorin, I. Rogachevskii, and I. Esau (2013), A hierarchy of energy- and flux-budget (EFB) turbulence closure models for stably-stratified geophysical flows, *Boundary Layer Meteorol.*, *146*(3), 341–373, doi:10.1007/s10546-012-9768-8.